Rouhollah Adinehvand and Ezzat Raeisi. Characterization of a karst aquifer in a complex tectonic region, Southwestern Iran. *Journal of Cave and Karst Studies*, v. 80, no. 4, p. 190-205. DOI:10.4311/2017ES0107

CHARACTERIZATION OF A KARST AQUIFER IN A COMPLEX TECTONIC REGION, SOUTHWESTERN IRAN

Rouhollah Adinehvand[1] and Ezzat Raeisi[2,C]

ABSTRACT

Characterization of karst aquifers is not unique and depends on geological and structural settings, relief, precipitation, and the interactions of these parameters. Therefore, the characterization of a highland karst aquifer in tectonized geological settings is still a challenge, especially in a region with scarce hydrogeological data. In this study, we characterize an inaccessible highland karst aquifer under the severe compressional stresses of two thrust faults, using extensive hydrogeological data by an integrated approach. The Malagha karst aquifer is located in the southern limb of the Malagha Anticline in a tectonized highland zone and is bounded by the Malagha and Qale-Tol thrust faults. Dam construction-related data including hydrochemical data, stable isotopes, water table levels, geological logs, permeabilities, fracture zones from numerous boreholes, and data from three dye tracer tests were used to evaluate the aquifer behavior. The exposed breccia zones and the significant water table differences on both sides of the Qale-Tol thrust fault core confirm the barrier behavior of the fault. The damage zone is highly fractured based on the geological logs, resulting in a relatively uniform water level distribution. The karst water flows through the extensive fracture networks inside the damage zone with no evidence of converging toward any main conduit. The type of flow is most probably diffuse, based on two dye tracer tests, the flat water table, and continuous high permeabilities up to a length of 140 m. The general flow direction is parallel to the fault strike, toward the downstream alluvium bounded between two impermeable formations. This conclusion is based on water balance, geological settings, and $\delta^{18}O$ and $\delta^{2}H$ data. Due to the flatness of the water table, such conditions as the mound below the Abolabbas River, bedding plane dips, and fractures and joints may locally control the flow direction. The footprint of the karst water and the recharge from the Abolabbas River are distinguishable by the hydrochemical and isotopic data.

Introduction

A karst aquifer is a complex heterogeneous medium because its characteristics are controlled by several factors including tectonic and stratigraphic settings, precipitation, temperature, and local and regional base levels. These parameters vary significantly between different karst aquifers, especially in active tectonic zones. Deep knowledge of karst aquifers is very important for drinking, industrial, and agricultural karst water uses and selection of dam sites or tracing contaminants.

Reviewing research on the effects of faults on non-karstic formations is required to understand the actions of the faults on karst aquifers. Faults control the aquifer hydraulic behavior and the groundwater flow pattern (Bense et al., 2008; Mayer and Sharp, 1998; Bense and Person, 2006; Mayer et al., 2007) Fault zones usually consist of a fault core that is surrounded by a damage zone cutting through the un-deformed host-rock, or protolith (Chester and Logan, 1986; Caine et al., 1996; Bense et al., 2013). The protolith may contain background joints, not primarily related to the fault zone (Bense et al., 2013). The fault core is the zone of the most intense strain and refers to intensely deformed materials which strongly reduce porosity and permeability compared to the adjacent damage zone and protolith (Chester and Logan, 1986; Antonellini et al., 1994; Goddard and Evans, 1995). Therefore, fault cores may act as low-flow or no-flow boundaries (Caine et al., 1996). The damage zone has secondary structures such as fractures and minor faults which take up the remainder of the strain within the fault zone (Bense et al., 2013) and causes heterogeneity and anisotropy in the permeability of the fault zone (Bruhn et al., 1994; McGrath and Davison, 1995). The secondary structures enhance permeability relative to the fault core and the host-rock (Chester and Logan, 1986; Goddard and Evans, 1995; Bense et al., 2013; Solum and Huisman, 2016). The damage zones form permeable fractures which are mostly oriented parallel to the fault plane (Caine et al., 1996). The permeability of the damage zone is significantly increased due to high fracture density and connectivity and is generally higher than that of the protolith (Bense et al., 2013).

Structural geologists use various methods, such as outcrop mapping of fault zones (Caine and Forster, 1999; Jourde et al., 2002; Shipton et al., 2005), mineralogy and geochemistry studies (Caine and Minor, 2009; Koukouvelas and Papoulis, 2009) , and porosity and permeametry measurements on cores in the laboratory or in the field (Antonellini et al., 1994; Faoro et al., 2009). Hydrogeological methods of studies of the fault zones include subsurface studies such as permeability by pumping tests (Anderson and Bakker, 2008), determination of hydraulic gradients on both sides of the fault core (Bense and Van Balen, 2004), artificial environmental tracer delineating fluid flow paths (Rugh and Burbey,

[1] Department of Earth Sciences, Shiraz University, Shiraz, Fars Province, Iran; radinehvand66@yahoo.com
[2] Department of Earth Sciences, Shiraz University, Faculty of Science, 7146713565; Shiraz, Fars Province, Iran,;
[C]Corresponding author: e_raeisi@yahoo.com

2008; Leray et al., 2012) and numerical models (Caine and Forster, 1999; Jourde et al., 2002; Surrette and Allen, 2008). Hydrogeologists often characterize karst aquifer hydrodynamics without a specific focus on fault zones (Celico et al., 2006; Doan and Cornet, 2007; Apaydin, 2010), in contrast to structural geologists who are mainly focused on fault zone characteristics (Caine et al., 1996; Billi et al., 2003). In literature, the links between the hydrogeological and structural viewpoints, especially in highland tectonized zones, are limited. Bense et al. (2013) extensively reviewed the hydrogeology of fault zones based on both structural and hydrogeological approaches.

In carbonate rocks, cataclasite, ultracataclasite, fault gouge (Agosta and Kirschner, 2003; Billi et al., 2003; Ferrill and Morris, 2003; Kostakioti et al., 2004; Micarelli et al., 2006; Benedicto et al., 2008; Billi, 2010; Tesei et al., 2013), clay smear and fluid flow cementation (Micarelli et al., 2006; Kim and Sanderson, 2010) reduce permeability of the fault cores. In karstic carbonate aquifers, the impermeable fault cores impede the flow perpendicular to the core and direct the flow parallel to the fault plane in the damage zone, creating a significant head difference, for example 5 m to 7 m (Celico et al., 2006) and 40 to 100 m (Cappa et al., 2005, 2007; Hamaker and Harris, 2007; Micarelli et al., 2006; Doan and Cornet, 2007; Apaydin, 2010 on both sides of the fault cores. Faults in carbonate rocks display a complex hydrogeological behavior, from barriers by secondary cementation or smearing of low permeability material in the core to conduits developed by the dissolution process in fractured dominantly damage zone (Bense et al. 2013). The productive Edwards Aquifer in south-central Texas, USA, formed in Cretaceous limestones is another example of active karst regions (Maclay, 1995; Ferrill et al., 2004). The karst groundwater flow in the aquifer is controlled by the Balcones fault system, a system of high-angle normal faults (Ferrill et al., 2004). Faulting had a critical role in the aquifer evolution (Lindgren et al., 2004), through solution enlargement of fractures and forming caves along faults (Hovorka et al., 1998). The faults strongly control cave orientation (Wermund et al., 1978; Alexander, 1990) and flow direction (Lindgren et al., 2004). Alpine karst in Europe can be divided into two main karst type, the plateau-like karst massifs (deep karst) and the folded alpine karst (shallow karst) based on geological and tectonical structures (Goldscheider and Hoetzl, 1999). As part of the Alpine fold and thrust belt, the strata are affected by polyphase deformation and the tectonics is very complex in high alpine karst plateaus (Plan et al., 2009). Faults are a main factor controlling drainage patterns of thick carbonate sequences in the south of Alpine and Austroalpine zones (Hoetzl, 1998; Goldscheider and Neukum, 2010) . Cave patterns and groundwater flow paths often follow faults and fractures within the karst limestones (Goldscheider, 2005; Goldscheider and Neukum, 2010) and cross-formational flow between karst aquifers separated with marl formations is demonstrated (Gremaud et al., 2009).

The studied karstic Malagha Aquifer is located in the High Zagros Zone in southwestern Iran, a tectonized highland zone, which is characterized by northwest-trending asymmetric anticlines, synclines and high-angle reverse faults. The Malagha Aquifer is formed in the highly fractured karstic Asmari Formation (AF) of the overturned southern limb of the Malagha Anticline (Fig. 1a and Fig. 1b). The objective of this study is to investigate the hydrogeological behavior of the Malagha karst aquifer within a highly tectonized region, using integration of extensive hydrogeological data. The combination of these specific methods finally enables us to propose a conceptual model of the aquifer.

Hydrogeological Settings

The karstified carbonate rocks crop out on about 23 % of the Zagros Mountains in the south-central regions of Iran (Nassery, 1991; Raeisi and Kowsar, 1997). The Zagros Mountain ranges have been divided into three zones: High Zagros, Simply Folded Belt, and Khuzestan Plane (Stocklin, 1968; Falcon, 1974; Berberian and King, 1981) . In these regions, most of the hydrogeological and hydrochemical studies on karst aquifers are on the Simply Folded Belt (Raeisi and Karami, 1997). The study area is located on the border between the High Zagros Zone and the Simply Folded Belt inside the Izeh Zone, a tectonized complex zone (Sepehr and Cosgrove, 2004; Sherkati and Letouzey, 2004; Sherkati et al., 2005) and its relationship to sedimentary facies and the evolution of sedimentary depocenters since Late Cretaceous times have been studied, on the basis of one regional balanced transect and several updated isopach maps, in the Izeh zone and the Dezful Embayment, central Zagros. This study relies on fieldwork data, existing geological maps, seismic data and well information. A new structural classification for part of the Zagros sedimentary cover is presented to highlight the different mechanical behavior of the formations in the stratigraphic column. It shows the existence of several local decollement levels activated during folding. These decollement levels separate lithotectonic units, which accommodate shortening in different ways. The Lower Paleozoic is the basal decollement level throughout the studied area. Triassic evaporites, Albian shales, Eocene marls and Miocene evaporites can act as intermediate decollement levels, and present variable facies in the Central Zagros. Lateral facies and thickness variations, the sedimentary overburden and the close relationship with inherited fault patterns influenced the wavelength, amplitude and style of folding in the study area. Furthermore, surface structures do not necessarily coincide with deeper objectives where these disharmonic levels are involved in folding. The evolution of sedimentary depocenters from the Late Cretaceous (obduction episode. The High Zagros Zone is bounded to the northeast by the Main Zagros thrust fault, and in the southwest, it is separated from the Zagros Simply Folded Belt by the seismically active High Zagros Fault (Berberian, 1995). To the southwest,

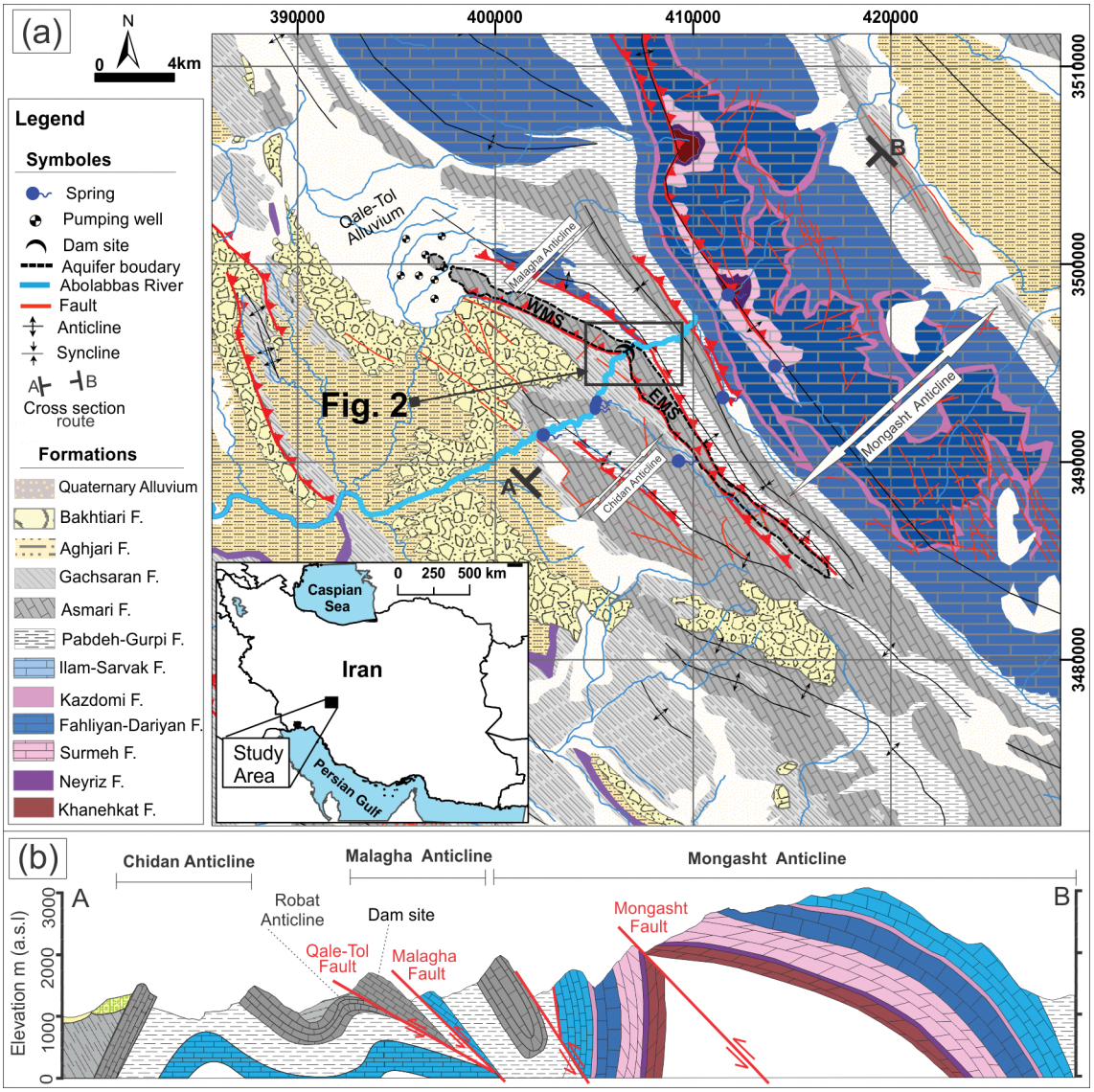

Figure 1. (a) General geological map of the study area. The boundary of the Malagha Aquifer is shown with dashed lines and its western and eastern sub-aquifers (WMS and EMS) in both sides of the Abolabbas River are pointed out in the figure. (b) A geological cross section near the dam site perpendicular to the Malagha Anticline has been drawn, showing the impact of faults on the formation of structures near the dam site and the surrounding geology.

the Zagros Simply Folded Belt is separated from the Khuzestan Plane by the Mountain Front Fault (Falcon, 1961). The Khuzestan Plain is composed of flat alluvial planes. The Simply Folded Belt is distinguished by long, linear, asymmetrical folds having a northwest to southeast trend. The anticlines are well-exposed and separated by broad valleys (Miliaresis, 2001; Ashjari and Raeisi, 2006). The faulting and thrusting in the High Zagros Zone has caused intensive rock deformation, crushing, elevated topography (up to 4000 m above sea level (a.s.l.)), and exposure of the oldest formations (Sherkati and Letouzey, 2004; Emami, 2008). Shortening, closed recumbent folds, and increasing faulting frequency are other characteristics of the High Zagros Zone (Berberian, 1995).

The climate of the study area is semiarid. The minimum, maximum and average annual precipitation are 379 mm, 907 mm, and 622 mm, respectively. Annual average evaporation is 1457 mm and daily temperature ranges from −1 °C to 41 °C (Mahab Ghodss Consulting Engineers, 2004). All precipitation occurs during November to May, mostly in the form of rain or snowfall (Najmeddin et al., 2017). The main exposed formations, in decreasing order of age, are Surmeh limestone (Oxfordian-Tithonian), Fahliyan-Dariyan limestone (Berriasian-Aptian), Sarvak-Ilam limestone (Cenomanian-Campanian), Pabdeh-Gurpi marl with thin interbeds of marly limestone (Paleocene-Oligocene), Asmari limestone (Oligocene-Miocene), Gachsaran marl, anhydrate, gypsum and salts (Lower Miocene), Aghajari marl and sandstone (Upper Miocene), and Bakhtiari conglomerates (Pleistocene) (Fig. 1a). In the study area, there are three anticlines as the main geological structures, namely the Mongasht, Malagha and Chidan (Fig. 1a). Three main reverse faults, Mongasht, Malagha, and Qale-Tol, parallel to the anticlines' axis, have been formed by compressional forces (Fig. 1b). The Mongasht Anticline, with the highest elevation in the study area, is an asymmetric tight fold with a short wavelength. The cores of the Mongasht and Malagha Anticlines are exposed due to faulting and erosion processes, in a way that the northern and southern limbs are disconnected and the older formations outcrop at the surface (Fig. 1a). The southern limbs of these two anticlines are overturned. The syncline between the Mongasht and Malagha Anticlines

is an overturned close fold. The Chidan Anticline is located near the border of the Simply Folded Belt. The Mongasht and Malagha are tight folds with short wavelengths compared to the Chidan Fold. The Robat Anticline is a small subsurface asymmetric anticline located between the Malagha and Chidan Anticlines (Fig. 1b).

Intensive tectonic activity has formed several parallel independent aquifers in the karstic Asmari, Fahliyan-Dariyan, and Sarvak-Ilam Formations at the northern and southern limbs of the Mongasht and Malagha Anticlines (Fig. 1a). The karst waters of these independent aquifers are mainly discharged through several springs (Adinehvand, 2017). The AF of the overturned southern limb of the Malagha Anticline has formed karstic Malagha Aquifer (Fig. 1a). The AR divided the Malagha Aquifer into the western and eastern parts or sub-aquifers. The parts of the Malagha Aquifer on the left and right sides (banks) of the AR and Malagha Gorge are named the Eastern and Western Malagha sub-aquifers, respectively (Fig. 1a). No springs emerge from the Malagha Aquifer. The karst waters of the aquifer discharge into the Qale-Tol alluvial aquifer at the western plunge of the Malagha Anticline, being exploited by several pumping wells (Fig 1a). The boundaries of the Malagha Aquifer are limited to impermeable Pabdeh-Gurpi and Gachsaran Formations from the northern and southern sides, and to the Qale-Tol alluvial aquifer and Chidan Anticline at the western and eastern plunges, respectively (Fig. 1a). There are no sinkholes, shafts, big caves, nor springs in the Malagha Aquifer. The karst features are grikes, rillenkarren, and rain pits. The sources of karst waters are autogenic recharge from precipitation through thin soil covers, fractures, grikes, and seepage from the AR bed. Parts of the Malagha Aquifer and Robat Anticline, upstream and downstream of the Qale-Tol thrust fault bounded by boreholes, are named the Dam-site Malagha Aquifer (DMA) and the Local Robat Aquifer (LRA), respectively (Fig. 2). The DMA is located in parts of the As1, As2 and As3 Units of the overturned southern limb of the Malagha Anticline (Fig. 2). The LRA is a small aquifer with an exposed area of about 0.05 km^2, formed in the As3 Unit of the northern limb of the Robat Anticline (Fig. 2). Both of these aquifers are unconfined.

The Abolabbas Dam under study, with a reservoir capacity of 113.4 Mm^3 and height of 138 m, is located inside the Malagha Gorge on the AF (Fig. 3). The dam will be constructed across the AR. The sources of the AR are three large karst springs, flood waters, and snowmelt from the Mongasht Anticline and the northern limb of the Malagha Anticline (Fig. 1a). The minimum, maximum and average discharges of the AR at the dam site are about 1 m^3/s, 8.8 m^3/s, and 2 m^3/s, respectively. Parts of Malagha Aquifer have been studied in detail already in order to design the Abolabbas Dam. The Mahab Ghodds Consulting Engineers (2004) classified the AF of the Malagha Aquifer into three units, namely the lower (As1),

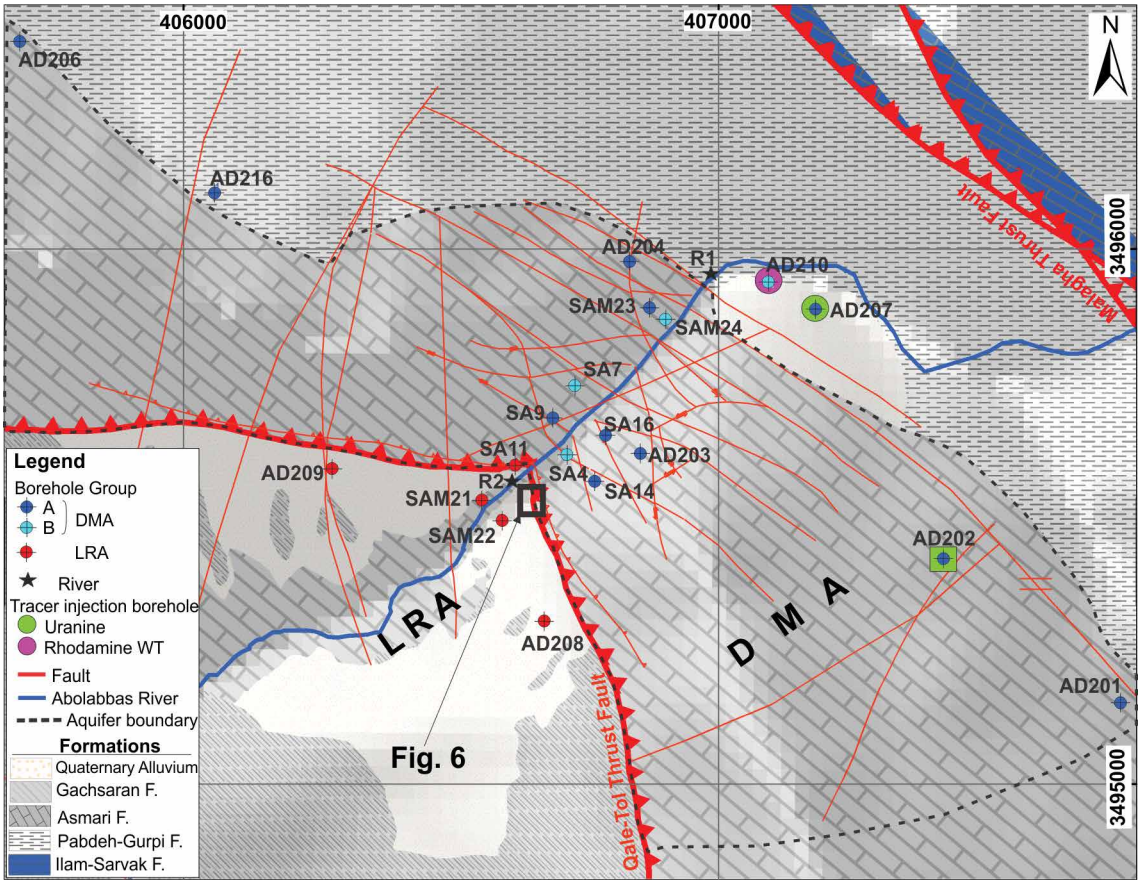

Figure 2. Geological map of the dam site and the location of the DMA and LRA boreholes. All the boreholes were used for water table monitoring and water sampling in the hydrogeochemical analyses and tracer tests. Dye injection boreholes are pointed out in the figure (green circle for the first test (uranine); the cyan circle for the second test (rhodamine WT); and the green square for the third test (uranine)). See also Figure 1a in for the location of Figure 2.

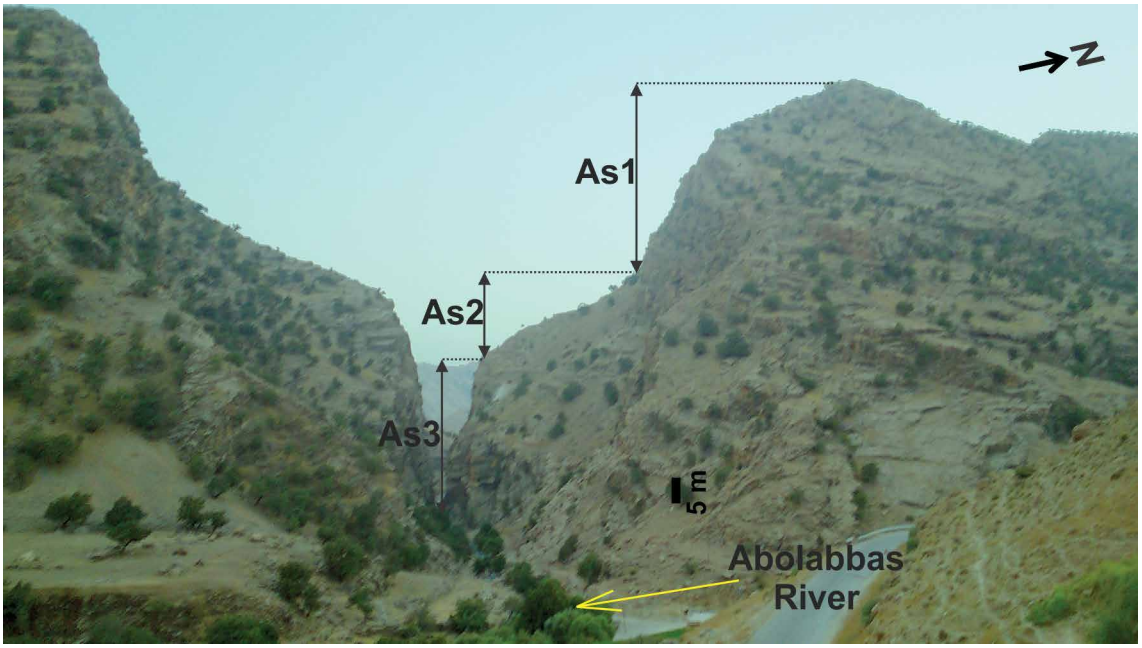

Figure 3. A photograph from the As1, As2 and As3 Units at the Malagha Gorge, where the Abolabbas Dam is planned to be constructed. The As2 Unit containing more marly limestone and limy marlstone formed a smooth topography between As1 and As3 Units.

middle (As2) and upper (As3) Asmari, in decreasing order of age, based on morphological, lithological, and hydrogeological characteristics (Fig. 3). The As1 and As3 Units make cliffs, while As2 unit makes a gentle topography (Fig. 3). The As1 Unit, with a thickness of 110 m, is composed of thick to massive limestones. The main characteristics of this unit are intensive fracturing and jointing. The As2 Unit is divided into the As2-a, As2-b and As2-c Subunits. The As2-a Subunit, with a thickness of 33 m, is composed of thin to medium bedded limestones with marly limestone interbeds. The As2-b Subunit consists of 21 m of marly limestone to marlstone. The As2-c Subunit has a thickness of 26 m of sandy limestones, thin to medium-bedded crystalline limestone with marl interbeds. The As3 Unit, with 150 m thickness, is composed of thin to thick-bedded and massive microcrystalline limestones with intensive fracturing. The dam is planned to be constructed on this unit.

Materials And Methods

The hydrogeology of the area was studied by Shiraz University from 2010 to 2015 (Majd, 2011; Adinehvand, 2017). The boundaries of the Malagha Aquifer (Fig. 1a) was estimated using geological settings, water balances, and $\delta^{18}O$ and $\delta^{2}H$ compositions (Adinehvand, 2017). The average aquifer recharge was estimated using the following equation

$$V = \frac{A \times P \times I}{t} \quad (1)$$

where V is the volume of recharge by precipitation (m^3/year), A is the aquifer surface area (10^{-6} km^2), P is the mean annual precipitation depth (10^3 mm), I is the recharge coefficient and t is one hydrological year. The precipitation depth (mm) at a specific elevation (m a.s.l.) was calculated using the precipitation-elevation relationship from 10 neighboring meteorological stations as follows,

$$P = 293.08 \ln H - 1356.7 \quad (2)$$

The mean annual precipitation ((10^3 mm)) over a specific area is calculated as follows,

$$\bar{P} = 10^{-3} \sum_{i=1}^{n} 293.08 \ln H_i - 1356.7 \quad (3)$$

where n is the number of 30 m by 30 m cells of the Digital Elevation Model (DEM) and H is the topographic elevation of each cell. The depth to the water level is at least 40 m below ground surface and therefore, evaporation from groundwater in neglected in the above calculations.

The flow rate of the AR was measured four times by a current-meter at the beginning and the end of the Malagha Gorge to determine the seepage from the river bed inside the Malagha Aquifer. Twenty boreholes were constructed on the eastern and western sides of the AR (Fig. 2; Table 1) by the Khuzestan Regional Water and Power Authority within the DMA and LRA and hydrogeological data were collected (Majd, 2011; Adinehvand, 2017). The lithology, permeability (lugeon) and fractures were measured at 5 m steps in these borehole logs.

Table 1. Hydrogeochemical data of the water samples.

Name	HCO3 (epm)	Ca (epm)	Mg (epm)	SO4 (epm)	Cl (epm)	Na (epm)	K (epm)	CO3 (epm)	TDS (mg/L)	EC (uS/cm)	Water-Type
Abolabbas River	3.40	3.06	1.69	0.97	0.38	0.05	0.02	0.05	226	290	Ca-HCO_3
Dam-site Malagha Aquifer											
Group A											
AD201	3.32	2.12	1.91	0.34	0.53	0.10	0.02	0.04	180	262	Ca-HCO_3
AD202	3.02	2.14	1.76	0.67	0.58	0.10	0.03	0.01	191	274	Ca-HCO_3
AD203	4.84	3.42	2.42	0.60	0.66	0.09	0.03	0.00	307	442	Ca-HCO_3
AD204	3.05	2.40	1.65	0.63	0.75	0.14	0.07	0.00	200	263	Ca-HCO_3
AD216	2.30	1.50	1.70	0.45	0.80	0.11	0.08	0.00	152	234	Mg-HCO_3
AD206	3.07	2.49	1.87	0.64	0.43	0.11	0.03	0.01	209	308	Ca-HCO_3
AD207	3.93	3.03	2.03	0.67	0.51	0.10	0.03	0.01	242	333	Ca-HCO_3
SA14	3.23	2.68	1.45	0.59	0.70	0.06	0.03	0.01	192	273	Ca-HCO_3
SA16	2.79	2.46	1.29	0.63	0.55	0.09	0.03	0.11	197	272	Ca-HCO_3
SA9	2.90	2.35	1.58	0.62	0.70	0.07	0.03	0.00	205	288	Ca-HCO_3
SAM23	3.10	2.70	1.80	0.48	0.65	0.07	0.04	0.00	225	315	Ca-HCO_3
Group B											
AD210	3.80	3.28	1.58	1.14	0.53	0.15	0.03	0.07	236	340	Ca-HCO_3
SA7	2.99	2.53	1.76	0.96	0.66	0.08	0.03	0.00	197	285	Ca-HCO_3
SA4	3.77	3.00	1.77	1.04	0.67	0.09	0.07	0.00	227	329	Ca-HCO_3
SAM24	3.74	3.20	1.87	0.99	0.58	0.06	0.02	0.00	235	331	Ca-HCO_3
Local Robat Aquifer											
AD209	3.30	2.70	1.50	0.67	0.50	0.09	0.04	0.00	216	332	Ca-HCO_3
AD208	3.44	6.03	2.50	4.58	0.64	0.13	0.03	0.02	515	625	Ca-SO_4
SA11	2.93	2.62	1.58	1.11	0.52	0.07	0.03	0.03	237	321	Ca-HCO_3
SAM21	1.60	1.22	0.82	0.08	0.58	0.35	0.08	0.12	119	141	Ca-HCO_3
SAM22	2.07	1.60	1.10	0.14	0.60	0.10	0.03	0.00	138	174	Ca-HCO_3

The water table levels were measured 19 times during the study period (2010 – 2015) in most of the DMA and LRA Boreholes (Fig. 2). The waters of the boreholes (DMA and LRA) and AR at the Malagha Gorge (Fig. 3) were sampled during the study period using USEPA (2007) and USGS (2006) guidelines. The pH, EC, and temperature were measured in the field, using portable instruments (WTW). The major anions and cations concentration and TDS were measured at the laboratory of the Department of Earth Sciences, Shiraz University. Major anion and cations concentration were analyzed based on methods of the American Public Health Association (APHA, 2005): sodium and potassium by flame photometer; calcium, carbonate, bicarbonate, and chloride by titration, while magnesium was calculated from the calcium contents, and the sulfates were estimated using the turbidity method. Stable isotope ^{18}O and ^{2}H compositions of six boreholes (AD201, AD202, AD207, AD208, SA7, and AD206) and the AR at the beginning and end of the Malagha Gorge (R1 and R2) were measured in the dry and wet seasons at the Freiberg Laboratory, Technische Universität Bergakademie, using the double mass spectrometry method (Fig. 2).

Three dye tracer tests, using fluorescent dyes, were performed in order to study the groundwater flow path and velocity within the Malagha Aquifer. In the first tracer test, 15 kg of uranine (MERK) were injected into Borehole AD207 (Majd, 2011) (Fig. 2). This borehole intersects the As1 Unit below the water table. In the second tracer test, 86 liters of Rhodamine WT (TURNER) was injected into Borehole AD210 in June 2014 (Fig. 2). This borehole intersects the As1 Unit below the water table. Forty kg of uranine (MERK) were injected into Borehole AD202 in the third tracer test (June 2014). This borehole intersects the As3 Unit below the water table. The sampling points of these three tracer tests were all boreholes inside the Malagha Aquifer (Fig. 2) and the pumping wells of the Qale-Tol plane (Fig. 1a). In addition, all the springs of the Chidan Anticline, as well as nine sections along the AR passing through the Malagha Gorge and Chidan Anticline, were also sampled (Fig. 1a). The time intervals of the samplings were once every hour and six hours from the sampling points near to and far from the injection wells, respectively, on the first day, which were gradually extended. The dye concentration was measured by a Shimadzu Spectrofluorophotometer, RF-5301PC, at the laboratory of the Department of Earth Sciences of Shiraz University.

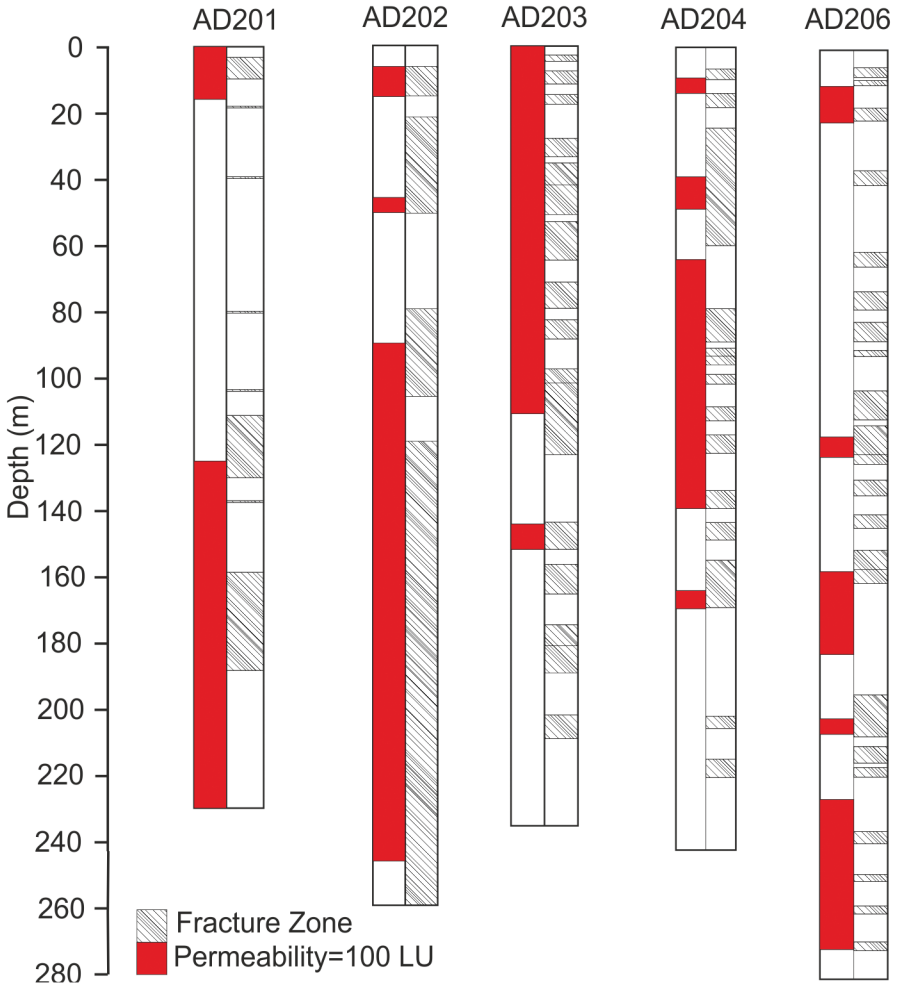

Figure 4. Permeability (lugeon) and fracture zones in the DMA boreholes.

Results

Aquifer recharge

Autogenic recharge from precipitation and seepage from the AR bed are the sources for karstic waters of the Malagha Aquifer. The areas of the Eastern and Western Malagha sub-aquifers are 11.2 km^2 and 8.0 km^2, respectively (Fig. 1a). The recharge coefficient *I* is estimated to be 50 ± 10 % based on the studies of the water balance in similar AF aquifers in the south west of Iran (Pezeshkpour, 1991; Rahnemaie, 1994) and other Mediterranean karst regions (Hartmann et al., 2014). Using Equation (1), the average annual recharge from precipitation on the Eastern and Western Malagha sub-aquifers, and the Malagha Aquifer are estimated to be 4.7 Mm^3, 2.9 Mm^3, and 7.6 Mm^3, respectively. The AR seeps into the karstic Malagha Aquifer along the Malagha Gorge. Four measurements of the AR flow rate at the beginning and end of the Malagha Gorge indicate an average seepage of about 83 Ls^{-1} (2.6 Mm^3y^{-1}) (Adinehvand, 2017). Therefore, the total recharge into the Malagha Aquifer is about 10.2 Mm^3y^{-1}.

The hydrogeology of the thrust faults

The hydrogeology of the DMA and LRA is controlled by the actions of Malagha, and especially the Qale-Tol thrust fault (Fig. 1b). The DMA is located in the damage zone of the Qale-Tol and Malagha thrust faults and LRA is located in the damage zone of the Qale-Tol thrust fault. The activity of these two thrust faults has resulted in extensive joints, fracture zones, and minor faults (Fig. 2). The extensive fracture zones are observed in some of the boreholes (Fig. 4) and limestone exposed areas (Fig. 5). The fracture zones in the boreholes have a significant correlation with continuous high permeabilities of 120 m length (Fig. 4). No cavity indicating a conduit was found in the high permeability sections of the boreholes (Adinehvand, 2017). The extensive fracture zones provide more pathways for groundwater flow than intact rock with less fractures which prevents the formation of a main flow pathway. Nonhomogeneous stress intensity causes a heterogeneity in the fracture zone distributions (Fig. 4) resulting in flow within the aquifer focus in the high permeability sections with extensively fractured zones. The Qale-Tol thrust fault core consists of breccia, gauge, cataclasite, and alterations in the exposed area (Fig. 6). The core of the Qale-Tol thrust fault acts as a barrier, disconnecting the hydraulic connection between the two sides of the fault core. The groundwater level differences in the LRA boreholes (AD209, SA11, SAM21, and SAM22) and in all boreholes of the DMA on both sides of the Qale-Tol thrust fault core are 10 m to 30 m (see the next section) which confirm the impermeable behavior of the fault core.

The Dam-site Malagha Aquifer (DMA) and Local Robat Aquifer (LRA)

Hydrogeochemistry

The chemical composition data in Table 1 gives an overview of the hydrogeochemical characteristics of groundwater in the DMA and LRA. The groundwater samples from DMA, LRA, and Abolabbas River are CaMg-HCO_3 type with TDS below 307 mg/L, EC of 442 μScm^{-1}, pH of 7.3, and temperature of 19.0 °C. The exception is AD208 in which the water type is Ca-SO_4 and TDS is 515 mg/L due to gypsum bearing veins in the borehole log. Groundwater temperature is almost constant in all water samples of the AR, DMA, and LRA.Groundwater samples from LRA show a significant

Figure 5. A photograph showing fracture zones on the limestones in the left side of the Malagha Gorge.

difference in hydrogeochemistry (Table 1). Even though the water type is mostly Ca-HCO_3, the EC varies from 141 to 625 µScm^{-1}. The lowest ion concentrations were found in SAM21 and SAM22 boreholes (Table 1). For all of the measurements during the monitoring period, the EC in both SAM21 and SAM22 boreholes was about 150 µScm^{-1}, which is at least 100 µScm^{-1} less than those of all the other boreholes and the AR (Table 1). The SO_4/Cl ratio of the water samples of the two boreholes is less than 1 and the major ions' concentrations are less than those of the AR and all of the other boreholes. The distances of the boreholes SA11, AD208, and AD209 from the AR are about 30 m, 150 m, and 230 m, respectively, and the SO_4/Cl ratio is higher than 1 similar to the AR. Based on the SO_4/Cl ratio in the water samples of the DMA boreholes, A and B groups can be distinguished (Fig. 7a, 7b). The SO_4/Cl ratio in the water samples of Group B boreholes is equal to or less than 1 (Fig. 7a) while in Group B boreholes it is higher than 1 (Fig. 7b). Group B boreholes have the closest distances from the AR and similar to the AR, the SO_4/Cl ratio is higher than 1 (Fig. 7b).

Stable isotopes

Stable isotope compositions for $\delta^{18}O$ and $\delta^{2}H$ in water samples of the AR (R1 and R2), DMA (AD201, AD202, AD203, AD206, AD207, and SA7) and LRA (AD208) in dry and wet seasons are shown in Fig. 8. All the water samples in the $\delta^{18}O$ and $\delta^{2}H$ diagram can be placed into two distinct groups of A and B. Group B consists of the boreholes of the DMA which are close to the river, LRA, and river water. The $\delta^{18}O$ values of Group B change from -6.2‰ to -6.2‰ and $\delta^{2}H$ values change from −26.4 ‰ to −23.4 ‰ (Fig. 8). Group A includes water samples of the DMA boreholes which are further from the river (Fig. 2). The $\delta^{18}O$ values of Group B evolve from −5.7 ‰ to −4.3 ‰ and $\delta^{2}H$ values from −20.8 ‰ to −12.3 ‰ (Fig. 8). Most of the water samples fall above global meteoric water line (GMWL) and close to the local meteoric water line (LMWL) (Fig. 8). The river water originates from Mongasht Anticline in the north which has the highest elevations in the study area and its water samples tend to have the most depleted $\delta^{18}O$ and $\delta^{2}H$ compositions (Fig.

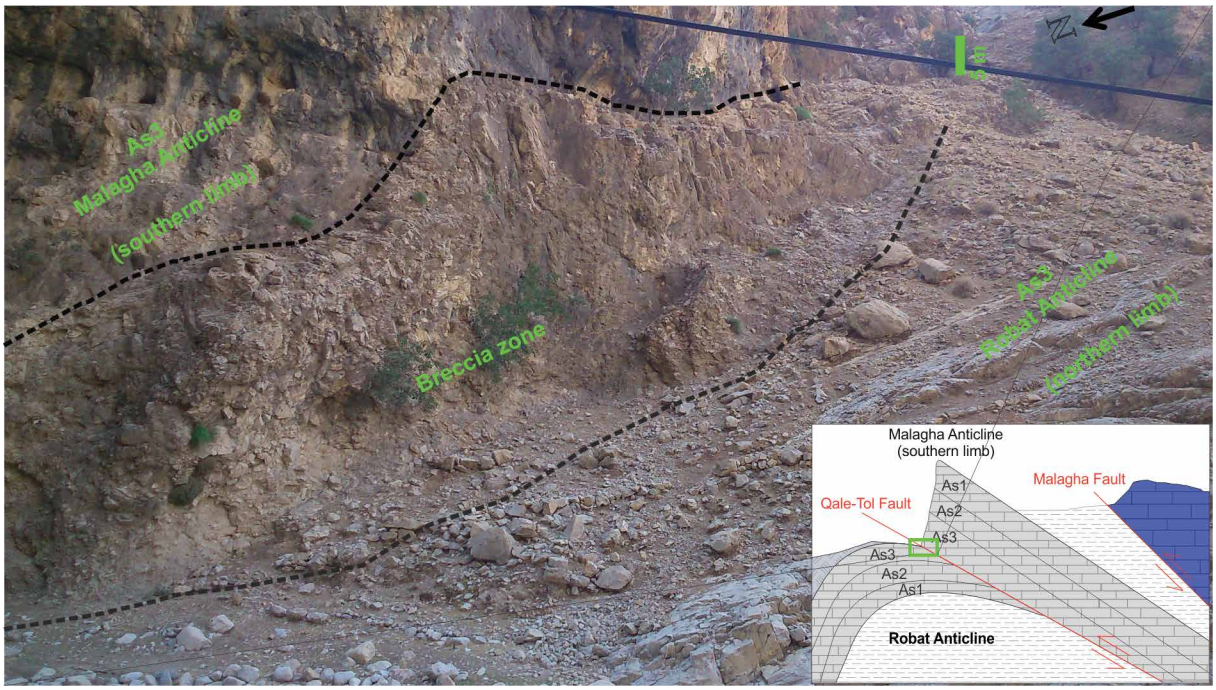

Figure 6. A photograph from breccia zone of the Qale-Tol Fault at the end of the Malagha Gorge. See Figure 2 for the location of Figure 6.

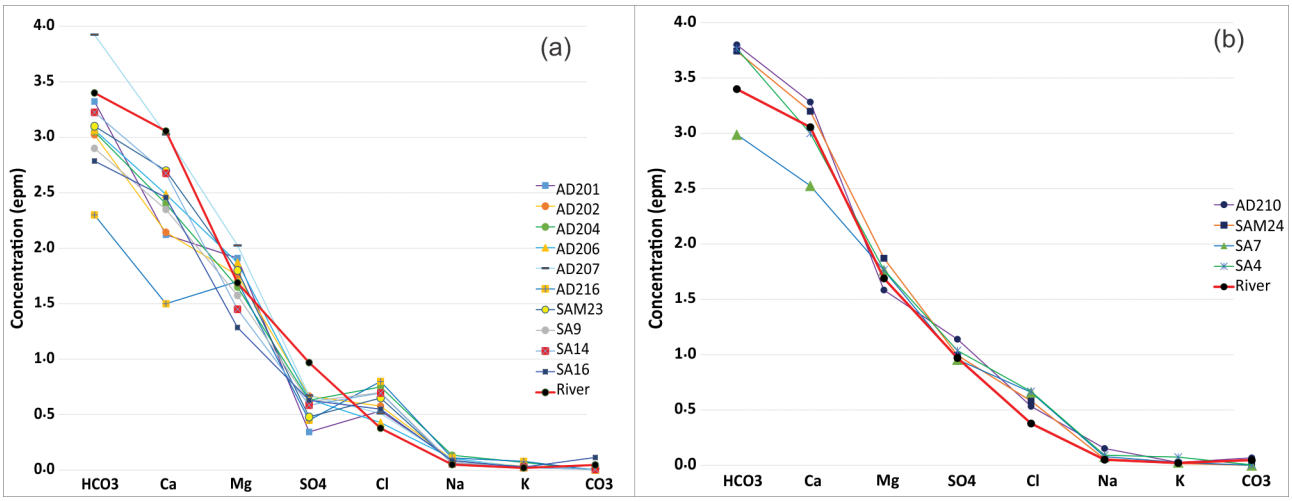

Figure 7. Water table map of the DMA and LRA boreholes. Major ion concentrations of the DMA boreholes; a) Group A, b) Group B.

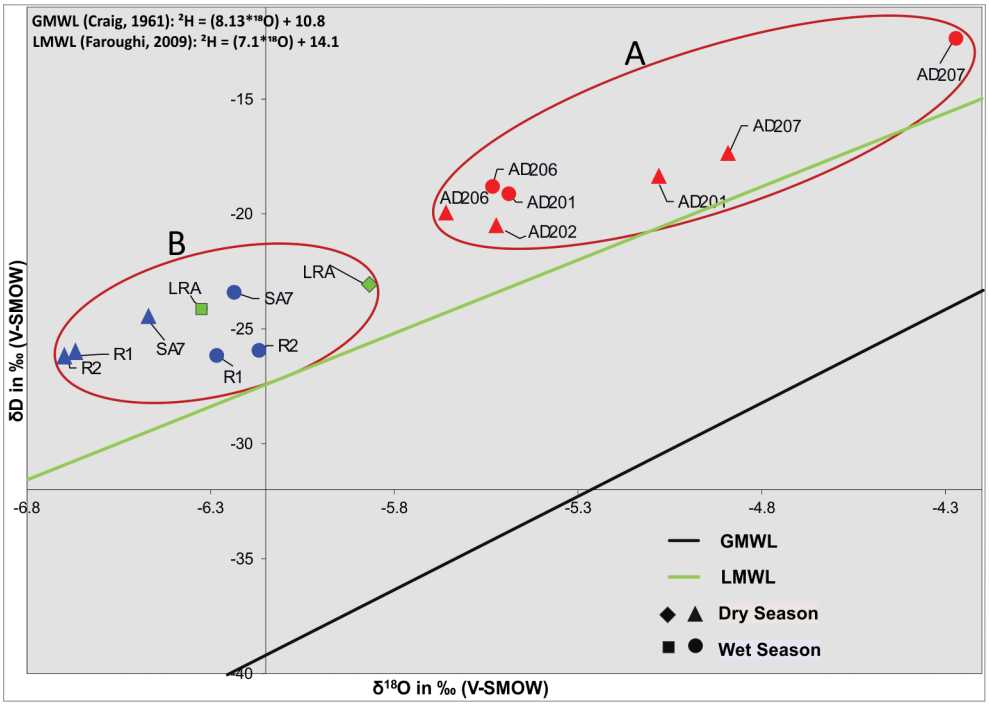

Figure 8. Stable isotope diagram of the DMA and LRA borehole water samples in dry and wet seasons. River water was also sampled at the entrance (R1) and exit (R2) of the Malagha Gorge. GMWL: global meteoric water line (Craig, 1961); LMWL: local meteoric water line (Faroughi, 2009).

8). Among the LRA boreholes, the $\delta^{18}O$ and $\delta^{2}H$ compositions were measured only for AD208. The $\delta^{18}O$ and $\delta^{2}H$ values are depleted and are in the range of the AR in the wet season and show a mixing component (Fig. 8). The water samples of the DMA boreholes which are close to the river show a mixing component and fall in the same group as the river (Group B) (Fig. 8). The waters of Group A tend to have more enriched compositions in $\delta^{18}O$ and $\delta^{2}H$ than those of Group B.

Water level distribution and fluctuation

Water level data were collected from all DMA and LRA boreholes with different time resolution measurements between June 2010 and August 2015 (Fig. 9). The DMA boreholes for water level monitoring include Group B boreholes (AD210, SA7, SA4, and SAM24), which are located close to the river, have slightly higher water levels, and may be affected by the river seepage, and Group A boreholes (AD201, AD202, AD203, AD204, AD216, AD206, AD207, SA14, SA16, SA9, and SAM23), which are farther from the river (Fig. 2). The LRA boreholes (SAM21, SAM22, SA11, AD208, and AD209) are located downstream of the Qale-Tol fault core, inside the gentle-dip bedding planes of the northern limb of the Robat Anticline (Fig. 1b, Fig. 2). The variations of the water level in each aquifer (DMA and LRA) differ. The water level in the LRA boreholes is 10 to 30 m higher than that of DMA (Fig. 9). The bottom elevations of all LRA boreholes are below the minimum DMA water table level. Therefore, the LRA boreholes are not located in a perched water table aquifer. The minimum, maximum, and average water level differences of the LRA boreholes are 13.4 m, 21.2 m, and 18.2 m, respectively, at a specific time during the monitoring period (Fig. 9). The boreholes SAM21 and SAM22 are located on both sides of the AR, with distances of less than 30 m (Fig. 2). The average of the water table levels of these boreholes is 989.50 m a.s.l., which is the highest among the LRA boreholes (Fig. 9). Groundwater level distributions in the LRA boreholes are highly variable, which is common in a karst aquifer.

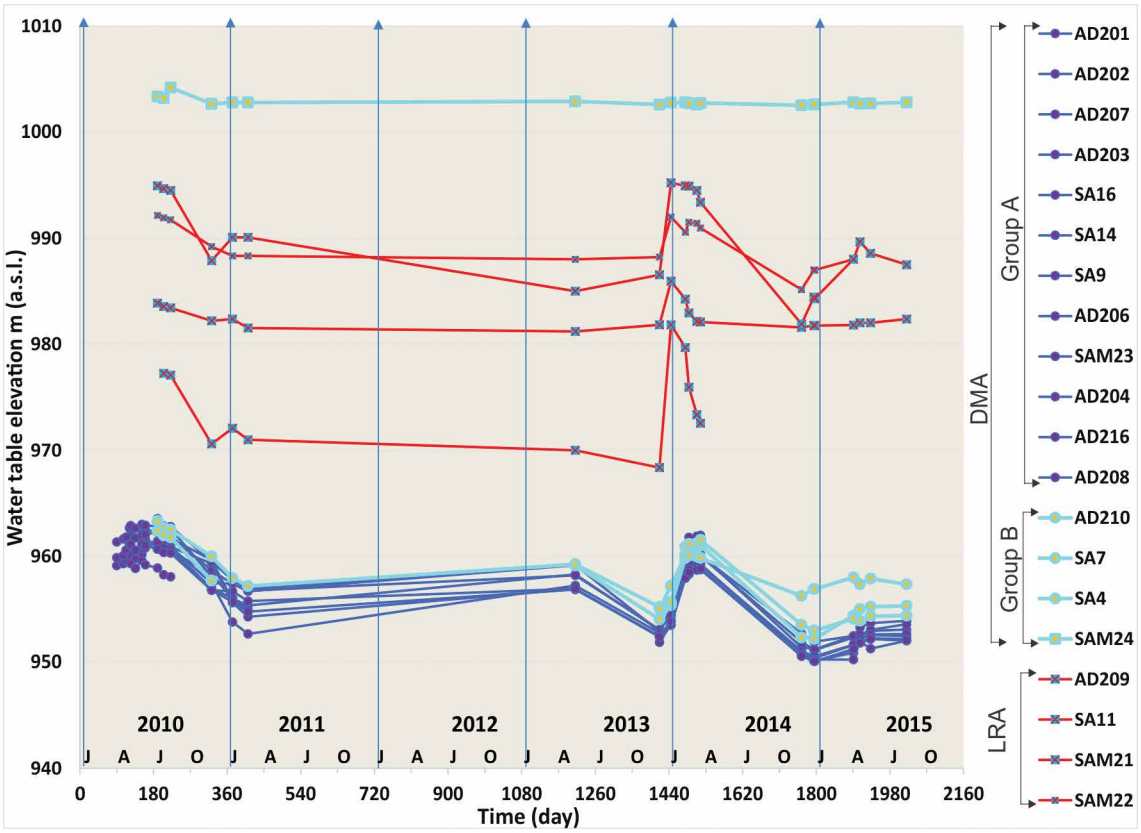

Figure 9. Water level elevation hydrographs in the DMA (Groups A and B) and LRA boreholes.

The water levels of the DMA boreholes are about 60 m below the river bed elevation. The minimum, maximum, and average water level differences of the DMA are 1.2 m, 4.7 m, and 2.8 m, respectively, at a specific time during the monitoring period (Fig. 9). The distances of Group B boreholes from the AR are less than 30 m, while the distances of Group A boreholes from the AR are more than 30 m (Fig. 2). The water table levels in Group B are always slightly higher than those of Group A during the monitoring period (Fig. 9), except for Borehole SAM24 in which the water table level is 45 m higher than that of Group A since it has the closest distance to the AR and has the lowest permeability. Although all of the boreholes of Groups A and B intersect with As1 and/or As3 below the water level, the water-level topography in the DMA is almost flat and shows an almost uniform distribution (Fig. 10a and 10b) similar to granular aquifers. Even though groundwater level measurements are relatively infrequent in time and also have different time resolutions, they can give some valuable information on aquifer homogeneity in space. To show the aquifer heterogeneous behavior more, simultaneous groundwater levels are drawn in the form of a cross-section connecting piezometers AD201 to AD206 as shown in Fig. 10a. The topography of water level is almost flat. To have a better understanding of flow direction in space, a groundwater elevation map for a specific time (July 30, 2014) is also drawn (Fig. 10b). The water level differences are less than 2.5 m and there is no preferential flow direction which shows the effect of the local heterogeneity in permeabilities within the aquifers (Fig. 4). The local flow has different and occasionally opposite directions (Fig. 10b).

Tracer tests

An overview of the locations and results of the three tracer tests is given in Table 2. In the first tracer test, uranine dye was injected into the Borehole AD207, intersecting the As1 Unit below the water table (Fig. 3), but it was not detected in any of the sampling points (Majd, 2011) (Table 2). The new Borehole AD210, intersecting the As1 Unit, was constructed for the second tracer test (Fig. 2). In the second tracer test, rhodamine WT dye was injected into Borehole AD210 and it was detected only in Borehole AD207 with a maximum velocity of 0.40 m/h, indicating a laminar flow regime (Table 2). In the third test, uranine dye was injected into the Borehole AD202 (Fig. 2), intersecting As1 and As2 from above, and As3 from below the water table level. The dye was only detected in Borehole AD207 at a distance of 550 m from the injection point (Fig. 2). The first and peak dye appearances occurred 76 days and 215 days after the dye injection, respectively. The maximum velocity was 0.62 m/h (Table 2), indicating a laminar flow regime.

DISCUSSION

The Dam-site Malagha Aquifer (DMA) and Local Robat Aquifer (LRA)

The hydrogeological study of the DMA and LRA is a suitable method to recognize the behavior of aquifers in a complex tectonic region. Part of the AR water seeps vertically into the DMA and forms a mound below the river and it

Table 2. Summary of qualitative and quantitative analysis tracer-tests.

Tracer Test	Dye Type	Injection Borehole	Detection Point	Migration Distance (m)	Maximum Velocity (m/h)	Peak Velocity (m/h)
First	Uranine	AD207	N/A	...	...	...
Second	Rhodamine WT	AD210	AD207	85	0.40	0.31
Third	Uranine	AD202	AD207	520	0.62	0.14

Sampling Stations: AD201, AD202, AD203, AD204, AD216, AD206, AD207, SA14, SA16, SA9, SAM23, AD210, SA7, SA4, SAM24, AD209, AD208, SA11, SAM21, SAM22, Abolabbas River (see Fig.2), Qale-Tol wells and Chidan springs (see Fig.1a).

is expected that the boreholes near the AR are under the influence of the mound. The sources of water of the DMA are seepage from the AR and precipitation recharge. The mixing of the AR with Eastern Malagha sub-aquifer water is a very complex process in a heterogeneous karst system. The boreholes of the DMA are classified into the two groups of A and B based on the share of the AR seepage (Fig. 3). Group A consists of boreholes AD201, AD202, AD203 AD207, SA14, SA16, SA9, SAM23, AD204, AD216, and AD206 while the boreholes of Group B are AD210, SA4, SAM24, and SA7 (Fig. 3). The water source of the boreholes of Group A is mainly recharge from precipitation, but the boreholes of Group B are dominantly under the direct influence of river seepage due to the following reasons:

1. The boreholes of Group B have shorter distances to the AR than the boreholes of Group A (Fig. 2).
2. The water table levels in Group B are always slightly higher than those of Group A (Fig. 9).
3. Similar to the AR, the ratio of SO_4/Cl in all water samples of Group B is more than 1, whereas, in Group A, it is less than or near 1 (Fig. 7).
4. The $\delta^{18}O$ and $\delta^{2}H$ compositions of the AR with a higher elevation than the Malagha Aquifer and Group B boreholes have the same range on the $\delta^{18}O$ and $\delta^{2}H$ diagram (Fig. 8), while they are enriched in Group A.

Group B boreholes are mainly located in the AR mound area. The mound is formed because the vertical flow of the AR seepage requires an extra head. Because of this, the water table levels of Group B boreholes cannot be used to determine the general flow direction of the DMA. The water table levels of Group A boreholes in the DMA are undulated without any trend to determine the flow direction. The extensive fracture zones caused a large cross-sectional area of flow, resulting in a low hydraulic gradient in the DMA. The uniform distribution and almost flat water-level topography in the DMA (Fig. 10a and 10b) indicate that the DMA has a behavior similar to those of the aquifers with more homogenous media (Bonacci, 1995; Bonacci and Roje-Bonacci, 2000; Kresic, 2010).

In all three dye tracer tests, the dye was not detected in the AR because the water levels in all of the sampling points were less than those of the river bed. The dye was not detected in any of the sampling points in the first tracer test (Majd, 2011). The reasons were the lack of any boreholes in the As1 Unit, and the time of injection being during the dry season (August 23, 2010) and a dry year. The closest boreholes (AD203) were located in the As3 Unit with a straight-line distance of more than 500 m from the injection borehole (AD207) which is located in the As1 Unit. This may indicate that there is no flow through the As3 Unit towards the AD203 Borehole and the dye probably flows only in the As1 Unit. The dye probably diluted and was absorbed by the rock matrix due to the long residence time of a laminar flow and fine materials of the crushed zones (Adinehvand, 2017). In the third tracer test, the dye may have flowed in the direction of the bedding planes slope through the As3, As2, and As1 Units and was detected in Borehole AD207 (Fig. 3). The dye was not expected to flow through the As2 Unit because it was composed of 21 m of marly limestone to marlstone, but this unit is permeable and does not act as an impermeable layer due to extensive fracturing. The dye has most probably been diluted and absorbed by fine crushed-materials in the media, similar to the first tracer test. It was expected that the dye in the third tracer test would flow parallel to the bedding plane strike in the As3 Unit and would be detected in borehole SA16, 600 m away from the injection borehole. The lack of dye detection in this borehole implies that there is no conduit flow in this direction.

The significant lower concentration of the major ions and EC in both of SAM21 and SAM22 boreholes than those of all the other boreholes and AR as well as the SO_4/Cl ratio which is less than 1 indicate that the source of the water is not the AR. The chemical characteristics of the water samples in SAM21 and SAM22 indicate that the source of water is probably local precipitation near the boreholes without a significant modification by water-rock interaction (Adinehvand, 2017). The unpredicted behavior of these two boreholes in such a complex tectonic setting merits further research. Despite their long distances from the AR, the main water source of the Boreholes SA11, AD208, and AD209 is probably the AR because: a) similar to the AR, the SO_4/Cl ratio is greater than 1; b) the exposed area of the LRA is limited; c) the Robat Anticline is covered by the impermeable Gachsaran Formation, and therefore, there is no recharge from precipitation, and; d) there is no flow from the DMA due to the Qale-Tol impermeable fault core and the DMA has a lower water table level.

Conceptual model and general flow direction

A conceptual model is proposed for the general flow direction and karst development of the DMA.

In a karst aquifer, groundwater in the intergranular pores in the rock matrix, fissures, fractures, and bedding planes flows towards the solutionally-connected conduits. The extensive fracture zones, continuous high permeabilities in the boreholes, flat and irregular water table, and laminar flow regime by two tracer tests imply no major conduit development and the karst water most probably flows in a network of solutionally-connected fractures. As mentioned earlier, extensive fracture zones were observed in the boreholes (Fig. 4) and several boreholes have a continuous permeability, up to 140 m length and 100 lu[1] (Fig. 4). There was no cavity in the high permeability sections of the boreholes (Adinehvand, 2017). The permeability of 100 lu in the boreholes with no cavity which have continuous lengths of 40 m to 140 m, indicating a distributed flow in the fracture zones. The extensive fracture zones with high permeabilities and no cavity reveal that no conduit has been developed to concentrate the karst water. In all the borehole logs no cavity, indicating the presence of conduits, was found, (Adinehvand, 2017). The water levels are irregular, which is expected in a karst aquifer. However, the differences between the DMA water levels are very low (Fig. 10a and Fig. 10b), and without any preferential direction toward channels or conduits. The almost flat, irregular, and uneven water table of the DMA implies a lack of large conduits to drain the karst water. The main reason is most probably the existence of extensive fracture networks in the DMA which make impermeable marly layers (AS2) more permeable, allow a cross-unit flow, and cause a flat water level by creating a large area of groundwater movement through joints and fractures. The extensive fracture and joints have caused the As2 Unit with a 21 m impermeable marly layer to lose its barrier role making this unit probably permeable because a) there were several boreholes intersecting the As2 Unit above the water table but there was no perched water table; b) dye moved from As3 Unit and then passed through As2 Unit in the form of a cross-unit flow and appeared in the As1 Unit (AD207 Borehole) in the third tracer test, and c) none of the boreholes showed a low permeability in the As2 Unit representing an impermeable marly layer. The existence of extensive fracture zones makes the media more permeable and creates more pathways for water movement. It causes the water to flow mainly through numerous fractures, preventing channelization of the water and formation of main karstic conduits. It seems that the flow is similar to those of alluvial aquifers but the water mainly flows through numerous solutional fractures instead of intergranular pores. The flow regime is laminar in spite of the high permeability of the dye injection and detection boreholes below the water table in the second and third tracer tests. The total area of intensive solutional fractures is so large that it reduces the discharge per unit area and velocity, resulting in a low hydraulic gradients and laminar flow regime. The results of the laminar flow regime in the DMA are compatible with the results from the semi-distributed model of Adinehvand et al. (2017).

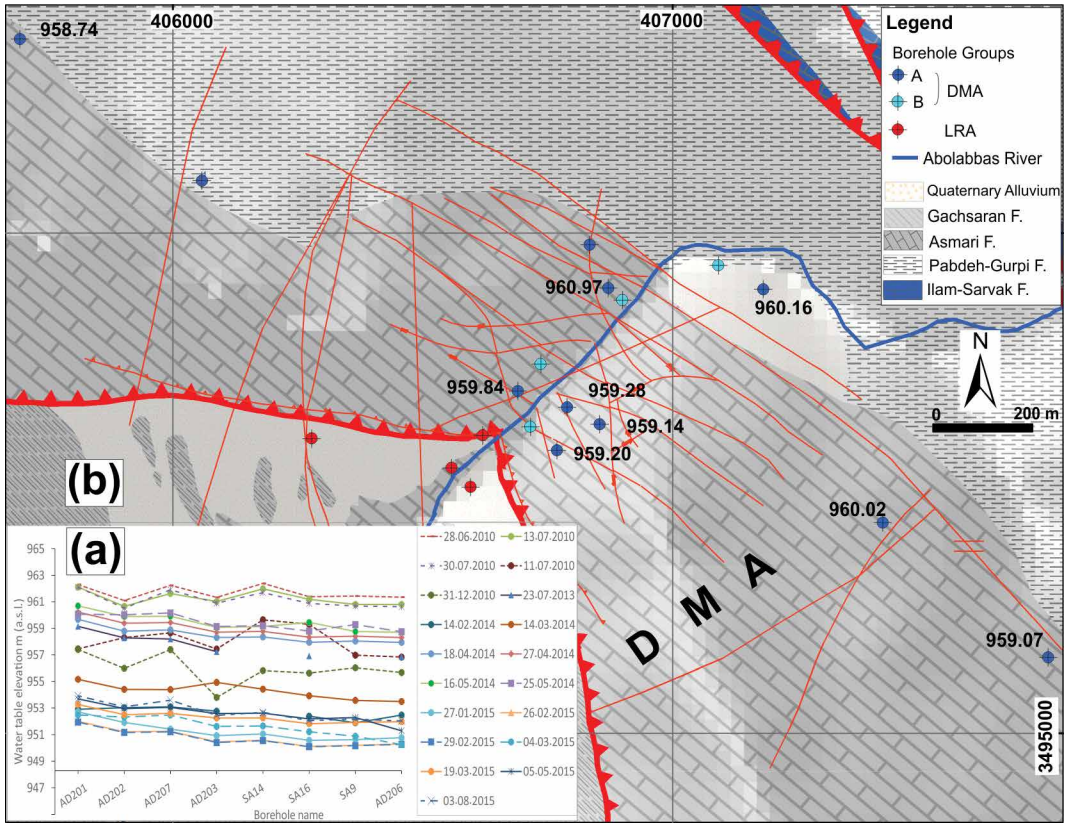

Figure 10. (a) Cross-sections of the simultaneous water levels in the direction of the general flow; (b) Water table elevation map for one of the simultaneous water level measurements shows an almost flat water table and a uniform distribution in the DMA.

The general flow direction is almost parallel to the Malagha Anticline bedding planes strike, toward the Qale-Tol alluvial aquifer (Fig. 11a). The karst water of the Eastern Malagha sub-aquifer is mixed with the AR and

[1] Editor's note: lu = Lugeon; 1 Lugeon Value (lu) = 1 Lmin^{-1} per meter of test interval under a reference pressure of 1 MPa.

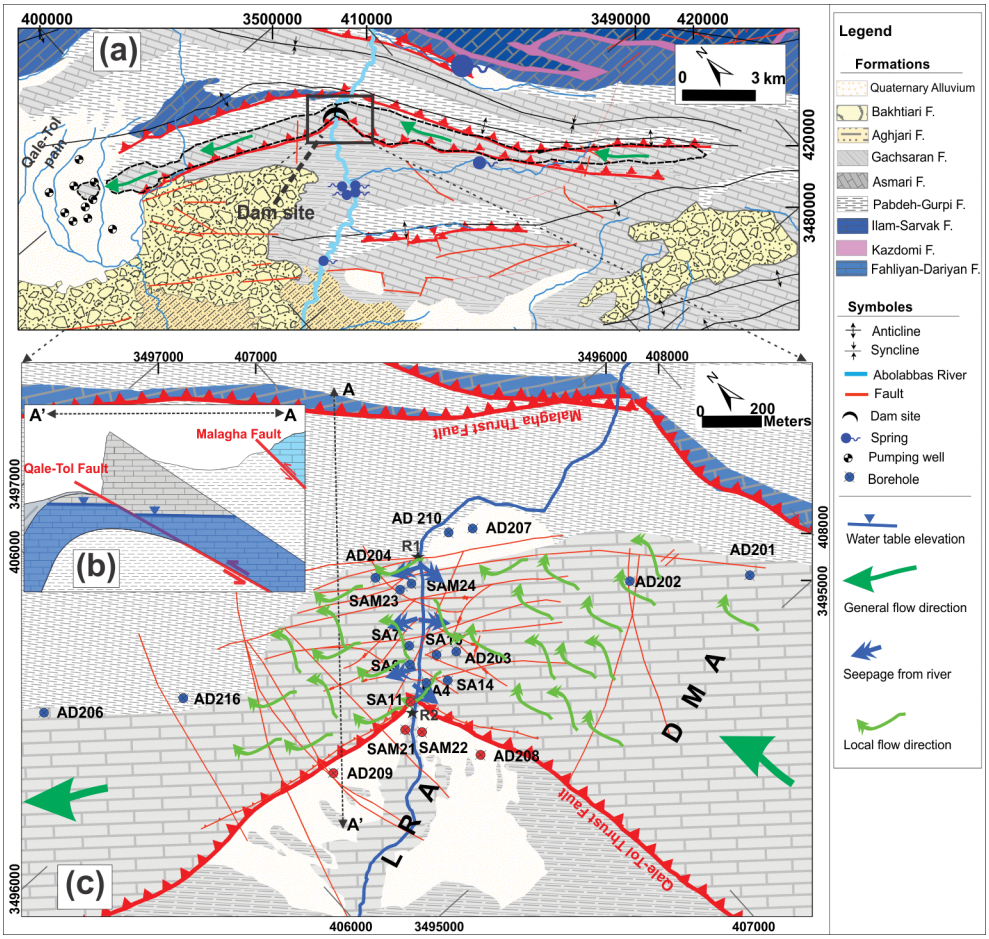

Figure 11. A schematic conceptual model proposing, (a) General flow direction in the Malagha Aquifer, (b) Water level in both sides of the Qale-Tol Fault core, and (c) General and local flow directions in the DMA.

the Western Malagha sub-aquifer, finally discharging into the Qale-Tol alluvial aquifer and is exploited by several wells. The following discussions confirm the proposed general flow direction. The flow direction across the Qale-Tol thrust fault is unlikely for two reasons. First, the core of the Qale-Tol thrust fault is impermeable and acts as a barrier and water levels in the DMA are lower than those in the LRA (Fig. 11b). Second, the water budget of the Chidan Aquifer indicates a balance between the recharge and discharge components (Adinehvand, 2017). The karst water of the Malagha Aquifer cannot be transferred toward the AF of the northern limb of the Malagha Anticline because: a) the connection of the northern and southern limbs is disconnected by the Malagha thrust fault and the impermeable Pabdeh-Gurpi Formations (Fig. 11a and Fig. 11b); b) the contact elevations of the northern limb of the Malagha Anticline with the adjacent Pabdeh-Gurpi Formations are significantly higher than those of the DMA water table. The flow direction is not toward the east because the contact elevations of the Malagha Aquifer with the Pabdeh-Gurpi and Gachsaran Formations are higher than the DMA water table and no springs emerge from the contact. Therefore, the karst water flow path is only toward the west, which is discharged by several exploitation wells in the Qale-Tol alluvial aquifer (Fig. 11a). In addition, the water levels of the DMA are about 110 m higher than those of the Qale-Tol Aquifer (Adinehvand, 2017), providing enough energy for groundwater movement. In spite of the general flow direction parallel to the Malagha Anticline axis, the karst water flow path may be locally controlled by the karst media heterogeneity of fracture networks (Fig. 4) and the river mound. Heterogeneities within the aquifer media may be evident in the form of different fracture intensities and permeabilities (Fig. 4). In such conditions, the flow direction may locally affect water flows towards nearby fractures with larger widths or areas with higher permeabilities and lead the water to flows in multiple directions (Fig. 11c). These factors are prominent, especially in an aquifer with a flat water table and low hydraulic gradient. The flow in the third tracer test is toward the contact of the Pabdeh-Gurpi Formations with low velocity, instead of towards the Malagha Gorge. The main reason is the greater thickness of the river mound below the AR than the thickness of the river mound below the impermeable Pabdeh-Gurpi Formations with further distances from the river. The existence of the mound under the AR may cause water to move towards parts of the DMA below the Pabdeh-Gurpi Formations which have a negligible mound.

Conclusions

This study integrated various and extensive data such as water table levels, hydrochemistry, stable isotopes, dye tracings, borehole logs (permeability and fracture zones), and geological settings to characterize a tectonized highland karst aquifer. The studied karst aquifer is located in the southern limb of the tectonized Malagha Anticline at the High Zagros Zone, bounded by the Malagha and Qale-Tol thrust faults. The impact of these two faults, the river crossing the aquifer, the mound below the river, and a flat water table have all resulted in a complex karst aquifer. The extensive

hydrological data collected for the construction of the Abolabbas Dam have provided a good basis to study the karst aquifer. The water balance of the Malagha Aquifer indicates that there was no inflow or outflow from the adjacent aquifers. The sources of the Malagha Aquifer water were recharge from precipitation and/or seepage from the Abolabbas River. The footprints of the river water, precipitation recharge, and the mix of these two sources were determined using hydrochemistry, stable isotopes ($\delta^{18}O$ and $\delta^{2}H$), and the water table levels in the boreholes.

The faults have two distinct hydrogeological impacts on the studied karst aquifer. On the one hand, Qale-Tol fault core acts as a barrier. The water table level differences on both sides of the Qale-Tol fault core and the exposed breccia confirm the barrier behavior of the fault core. On the other hand, the extensive fracture zones caused marly layers of the As2 Unit to lose their impermeability role, allowing a cross-unit flow. The existence of fracture zones resulted in more homogeneous media with relatively uniform water levels by increasing the groundwater flow cross-sectional area which are where two independent aquifers have been formed in the upstream and downstream of the fault core, respectively. The LRA is a small aquifer close to the Qale-Tol fault core probably with no hydraulic connection to the DMA. The DMA is located in a damage zone with extensive fractures crushed zones and minor faults. The two tracer tests indicated the velocities that are in the range of the laminar flow regime, and hence, a lack of main conduits. The water table levels of the DMA were almost flat and irregular, indicating that the karst water flows through extensive fractures which increases the total cross-sectional area of the flow and consequently reduces the velocity and hydraulic gradient. The extensive fracture zones, continuous high permeabilities, flat and irregular water table, and laminar flow regime by tracer tests suggested that there was no major conduit development and the karst water most probably flows through a network of solutionally-connected fractures. It seems that the karst water is distributed within extensive solutional fracture networks, similar to groundwater flow in inter-granular pores of alluvial aquifers.

The general flow direction of the DMA is parallel to the Qale-Tol thrust fault strike, towards the surrounding alluvial aquifer. However, the local heterogeneities such as fractures with larger apertures, a mound below the river, or a bedding plane dip may locally control the flow direction. Two boreholes in the vicinity of the Abolabbas River had water tables higher than the main aquifer and their electrical conductivities were significantly less than those of the Abolabbas River and the DMA, implying that the hydrological behavior near the fault core was complex due to the numerous hydrological and structural processes occurring around the fault core. Most of the research carried out on tectonized highland aquifers have focused either on the fault zones from a structural geological point of view, or on water table differences on both sides of the fault core. Research on the hydrogeology of damage zones, especially on karst aquifers under the impact of thrust faults, is limited due to the lack of borehole or exploitation well data from such elevated and rough topographies. The proposed approach can also be useful in other tectonically active regions with scarce data to characterize complex and tectonized karst systems.

Acknowledgments

The authors acknowledge the Research Council of Shiraz University for their support of this work. We are grateful to Khuzestan Regional Power and Water Authority for their financial support. Special thanks are due to R. Averand and N. Damogh for helping with field work and data collection, to H. Zarei, M. Mahdavinejad and A. Negintaji for their cooperation on this project, and to A. Majd for providing parts of hydrogeological data and performing the first tracer test. The authors also thank Dr. Andreas Hartmann of the Institute of Hydrology, University of Freiburg for reviewing the first draft of the manuscript. Our thanks also go to the two anonymous reviewers for their constructive comments on the manuscript.

References

Adinehvand, R., 2017, Evaluation of water leakage potential from Abolabbas Karst dam site using Hydrogeology, Modeling and Dye Tracing Methods [Ph.D. dissertation]: Shiraz, University of Shiraz, 126 p.

Adinehvand, R., Raeisi, E., and Hartmann, A., 2017, A step-wise semi-distributed simulation approach to characterize a karst aquifer and to support dam construction in a data-scarce environment: Journal of Hydrology. v. 554, p. 470 -481, doi:10.1016/j.jhydrol.2017.08.056.

Agosta, F., and Kirschner, D.L., 2003, Fluid conduits in carbonate-hosted seismogenic normal faults of central Italy: Journal of Geophysical Research: Solid Earth, v. 108, p. 1–13, doi: 10.1029/2002JB002013.

Alexander, K., 1990, Correlation of structural lineaments and fracture traces to water-well yields in the Edwards Aquifer, Central Texas [Ph.D. dissertation]: The University of Texas at Austin, https://repositories.lib.utexas.edu/handle/2152/46325.

American Public Health Association (APHA), 2005, Standard methods for the examination of water and wastewater: American Public Health Association , 20st edn. American Water Works Association (AWWA) and Water Environment Federation (WEF), Denver, New Jersey.

Anderson, E.I., and Bakker, M., 2008, Groundwater flow through anisotropic fault zones in multiaquifer systems: Water Resources Research, v. 44, no. W11433, p. 1−11, doi: 10.1029/2008WR006925.

Antonellini, M.A., Aydin, A., and Pollard, D.D., 1994, Microstructure of deformation bands in porous sandstones at Arches National Park, Utah: Journal of Structural Geology, v. 16, p. 941–959, doi: 10.1016/0191-8141(94)90077-9.

Apaydin, A., 2010, Relation of tectonic structure to groundwater flow in the Beypazari region, NW Anatolia, Turkey: Hydrogeology Journal, v. 18, p. 1343–1356, doi: 10.1007/s10040-010-0605-1.

Ashjari, J. and Raeisi, E., 2006, Influences of anticlinal structure on regional flow, Zagros, Iran: Journal of Cave and Karst Studies, v. 68, no. 3, p. 118−129. doi

Benedicto, A., Plagnes, V., Vergely, P., Flotte, N., and Schultz, R.A., 2008, Fault and fluid interaction in a rifted margin: integrated study of calcite-sealed fault-related structures (southern Corinth margin): Geological Society, London, Special Publications, v. 299, p. 257–275, doi: 10.1144/SP299.16.Bense, V.F., Gleeson, T., Loveless, S.E., Bour, O., and Scibek, J., 2013, Fault zone hydrogeology: Earth-Science Reviews, v. 127, p. 171–192, doi: 10.1016/j.earscirev.2013.09.008.

Bense, V.F., and Person, M.A., 2006, Faults as conduit-barrier systems to fluid flow in siliciclastic sedimentary aquifers: Water Resources Research, v. 42, doi: 10.1029/2005WR004480.

Bense, V.F., Person, M.A., Chaudhary, K., You, Y., Cremer, N., and Simon, S., 2008, Thermal anomalies indicate preferential flow along faults in unconsolidated sedimentary aquifers: Geophysical Research Letters, v. 35, p. L24406, doi: 10.1029/2008GL036017.

Bense, V.F., and Van Balen, R., 2004, The effect of fault relay and clay smearing on groundwater flow patterns in the Lower Rhine Embayment: Basin Research, v. 16, p. 397–411, doi: 10.1111/j.1365-2117.2004.00238.x.

Berberian, M., 1995, Master “blind” thrust faults hidden under the Zagros folds: active basement tectonics and surface morphotectonics: Tectonophysics, v. 241, p. 193–224, doi: 10.1016/0040-1951(94)00185-C.

Berberian, M., and King, G.C.P., 1981, Towards a paleogeography and tectonic evolution of Iran: Reply: Canadian Journal of Earth Sciences, v. 18, p. 1764–1766, doi: 10.1139/e81-163.

Billi, A., 2010, Microtectonics of low-P low-T carbonate fault rocks: Journal of Structural Geology, v. 32, p. 1392–1402, doi: 10.1016/j.jsg.2009.05.007.

Billi, A., Salvini, F., and Storti, F., 2003, The damage zone-fault core transition in carbonate rocks: implications for fault growth, structure and permeability: Journal of Structural Geology, v. 25, p. 1779–1794, doi: 10.1016/S0191-8141(03)00037-3.

Bonacci, O., 1995, Ground water behaviour in karst: example of the Ombla Spring (Croatia): Journal of Hydrology, v. 165, p. 113–134, doi: 10.1016/0022-1694(94)02577-X.

Bonacci, O., and Roje-Bonacci, T., 2000, Interpretation of groundwater level monitoring results in karst aquifers: examples from the Dinaric karst: Hydrological Processes, v. 14, p. 2423–2438, doi: 10.1002/1099-1085(20001015)14:14<2423::AID-HYP104>3.0.CO;2-2.

Bruhn, R.L., Parry, W.T., Yonkee, W. a, and Thompson, T., 1994, Fracturing and hydrothermal alteration in normal fault zones: Pure and Applied Geophysics, v. 142, p. 609–644, doi: 10.1007/BF00876057.

Caine, J.S., Evans, J.P., and Forster, C.B., 1996, Fault zone architechture and permeability structure: Geology, v. 24, p. 1025–1028, doi: 10.1130/0091-7613(1996)024<1025.

Caine, J.S., and Forster, C.B., 1999, Fault zone architecture and fluid flow: Insights from field data and numerical modeling: Geophysical Monograph Series, v. 113, p. 101–127, doi: 10.1029/GM113p0101.

Caine, J.S., and Minor, S.A., 2009, Structural and geochemical characteristics of faulted sediments and inferences on the role of water in deformatiion, Rio Grande Rift, New Mexico: Bulletin of the Geological Society of America, v. 121, p. 1325–1340, doi: 10.1130/B26164.1.

Cappa, F., Guglielmi, Y., Fénart, P., Merrien-Soukatchoff, V., and Thoraval, A., 2005, Hydromechanical interactions in a fractured carbonate reservoir inferred from hydraulic and mechanical measurements: International Journal of Rock Mechanics and Mining Sciences, v. 42, p. 287–306, doi: 10.1016/j.ijrmms.2004.11.006.

Cappa, F., Guglielmi, Y., and Virieux, J., 2007, Stress and fluid transfer in a fault zone due to overpressures in the seismogenic crust: Geophysical Research Letters, v. 34, doi: 10.1029/2006GL028980.

Celico, F., Petrella, E., and Celico, P., 2006, Hydrogeological behaviour of some fault zones in a carbonate aquifer of Southern Italy: An experimentally based model: Terra Nova, v. 18, p. 308–313, doi: 10.1111/j.1365-3121.2006.00694.x.

Chester, F.M., and Logan, J.M., 1986, Implications for mechanical properties of brittle faults from observations of the Punchbowl fault zone, California: Pure and Applied Geophysics, v. 124, p. 79–106, doi: 10.1007/BF00875720.

Craig, H., 1961, Isotopic variations in meteoric waters: Science, v. 133, p. 1702–1703, doi: 10.1126/science.133.3465.1702.

Doan, M.L., and Cornet, F.H., 2007, Thermal anomaly near the Aigio fault, Gulf of Corinth, Greece, maybe due to convection below the fault: Geophysical Research Letters, v. 34, p. L06314, doi: 10.1029/2006GL028931.

Emami, H., 2008, Foreland Propagation of Folding and Structure of the Mountain Front Flexure in the Pusht-E Kuh Arc (Zagros, Iran) [PhD thesis]: Barcelona, Universitat de Barcelona, 180 p., http://hdl.handle.net/2445/34914.

Falcon, N.L., 1961, Major earth-flexing in the Zagros Mountains of southwest Iran: Quarterly Journal Geological Society of London, v. 117, p. 367–376.

Falcon, N.L., 1974, Southern Iran: Zagros Mountains: Geological Society, London, Special Publications, v. 4, p. 199–211, doi: 10.1144/GSL.SP.2005.004.01.11.

Faoro, I., Niemeijer, A., Marone, C., and Elsworth, D., 2009, Influence of shear and deviatoric stress on the evolution of permeability in fractured rock: Journal of Geophysical Research, v. 114, p. B01201, doi: 10.1029/2007JB005372.

Faroughi, A., 2009, Determination of isotopic characteristics of rain in Fars province: Shiraz University, 89 p.

Ferrill, D.A., and Morris, A.P., 2003, Erratum to: “Dilational normal faults”: Journal of Structural Geology, v. 25, p. 827, doi: 10.1016/S0191-8141(02)00196-7.

Ferrill, D.A., Sims, D.W., Waiting, D.J., Morris, A.P., Franklin, N.M., and Schultz, A.L., 2004, Structural framework of the Edwards Aquifer recharge zone in south-central Texas: Bulletin of the Geological Society of America, v. 116, p. 407–418, doi: 10.1130/B25174.1.

Goddard, J. V., and Evans, J.P., 1995, Chemical changes and fluid-rock interaction in faults of crystalline thrust sheets, northwestern Wyoming, U.S.A.: Journal of Structural Geology, v. 17, p. 533–547, doi: 10.1016/0191-8141(94)00068-B.

Goldscheider, N., 2005, Fold structure and underground drainage pattern in the alpine karst system Hochifen-Gottesacker: Eclogae Geologicae Helvetiae, v. 98, p. 1–17, doi: 10.1007/s00015-005-1143-z.

Goldscheider, N., and Hoetzl, H., 1999, Hydrogeological characteristics of folded alpine karst systems exemplified by the Gottesacker Plateau (German-Austrian Alps): Acta Carsologica, v. 28, p. 87–103.

Goldscheider, N., and Neukum, C., 2010, Fold and fault control on the drainage pattern of a double-karst-aquifer system, Winterstaude, Austrian Alps: Acta Carsologica, v. 39, p. 173–186, doi: 10.3986/ac.v39i2.91.

Gremaud, V., Goldscheider, N., Savoy, L., Favre, G., and Masson, H., 2009, Geological structure, recharge processes and underground drainage of a glacierised karst aquifer system, Tsanfleuron-Sanetsch, Swiss Alps: Hydrogeology Journal, v. 17, p. 1833–1848, doi: 10.1007/s10040-009-0485-4.

Hamaker, S., and Harris, R., 2007, Fault-related ground-water compartmentalization in the East Tintic Mining District, Utah: *in:* Willis, G.C., Hylland, M.D., Clark, D.L., and Chidsey, T.C., Jr., eds, Central Utah– Diverse geology of a dynamic landscape. Utah Geological Association Publications, Salt Lake City, Utah, v. 123, p. 405–423.

Hartmann, A., Mudarra, M., Andreo, B., Marín, A., Wagener, T., and Lange, J., 2014, Modeling spatiotemporal impacts of hydroclimatic extremes on groundwater recharge at a Mediterranean karst aquifer: Water Resources Research, v. 50, p. 6507–6521, doi: 10.1002/2014WR015685.

Hoetzl, H., 1998, Karst groundwater, *in* Kass, W. ed., Tracing Technique in Geohydrology, Balkema, p. 398–426.

Hovorka, S.D., Mace, R.E., and Collins, E.W., 1998, Permeability structure of the Edwards Aquifer, south Texas: implications for aquifer management: Bureau of Economic Geology, University of Texas at Austin.

Jourde, H., Pistre, S., Perrochet, P., and Drogue, C., 2002, Origin of fractional flow dimension to a partially penetrating well in stratified fractured reservoirs. New results based on the study of synthetic fracture networks: Advances in Water Resources, v. 25, p. 371–387, //000175890300002.

Kim, Y.-S., and Sanderson, D.J., 2010, Inferred fluid flow through fault damage zones based on the observation of stalactites in carbonate caves: Journal of Structural Geology, v. 32, p. 1305–1316, doi: 10.1016/j.jsg.2009.04.017.

Kostakioti, A., Xypolias, P., Kokkalas, S., and Doutsos, T., 2004, Quantitative analysis of deformation along the fault damage zone of the Klimatia Thrust (NW Greece, Ionian Zone): Bulletin of the Geological Society of Greece, v. XXXVI, p. 1643–1651.

Koukouvelas, I.K., and Papoulis, D., 2009, Fluid involvement in the active Helike normal Fault, Gulf of Corinth, Greece: Journal of Structural Geology, v. 31, p. 237–250, doi: 10.1016/j.jsg.2008.11.018.

Kresic, N., 2010, Modeling, *in* Kresic, N. and Stevanovic, Z. eds., Groundwater Hydrology of Karst Springs, Butterworth-Heinemann, p. 573.

Leray, S., de Dreuzy, J.-R., Bour, O., Labasque, T., and Aquilina, L., 2012, Contribution of age data to the characterization of complex aquifers: Journal of Hydrology, v. 464–465, p. 54–68, doi: 10.1016/j.jhydrol.2012.06.052.

Lindgren, R.J., Dutton, A.R., Hovorka, S.D., Worthington, S.R.H., and Painter, S., 2004, Conceptualization and simulation of the Edwards Aquifer, San Antonio Region, Texas. Scientific Investigations Report 2004 – 5277, 143 p. https://pubs.usgs.gov/sir/2004/5277/pdf/sir2004-5277.pdf

Maclay, R., 1995, Geology and hydrology of the Edwards Aquifer in the San Antonio area, Texas:, https://pubs.er.usgs.gov/publication/wri954186.

Mahab Ghodss Consulting, and Engineers, 2004, Climatology Report, The first stage: Mahab Ghodss Consulting Engineers (in Farsi).

Majd, A., 2011, Hydrogeological and dye tracing studies of Abolabbas dam, Khuzestan [MS. Thesis]: Shiraz, Shiraz University, 177 p.

Mayer, A., May, W., Lukkarila, C., and Diehl, J., 2007, Estimation of fault-zone conductance by calibration of a regional groundwater flow model: Desert Hot Springs, California: Hydrogeology Journal, v. 15, p. 1093–1106, doi: 10.1007/s10040-007-0158-0.

Mayer, J.R., and Sharp, J.M., 1998, Fracture control of regional ground-water flow in a carbonate aquifer in a semi-arid region: Bulletin of the Geological Society of America, v. 110, p. 269–283, doi: 10.1130/0016-7606(1998)110<0269:FCORGW>2.3.CO;2.

McGrath, A.G., and Davison, I., 1995, Damage zone geometry around fault tips: Journal of Structural Geology, v. 17, p. 1011–1024, doi: 10.1016/0191-8141(94)00116-H.

Micarelli, L., Moretti, I., Jaubert, M., and Moulouel, H., 2006, Fracture analysis in the south-western Corinth rift (Greece) and implications on fault hydraulic behavior: Tectonophysics, v. 426, p. 31–59, doi: 10.1016/j.tecto.2006.02.022.

Miliaresis, G., 2001, Geomorphometric mapping of Zagros Ranges at regional scale: Computers and Geosciences, vol. 27: p. 775-786, doi. org/10.1016/S0098-3004(00)00168-0

Najmeddin, A., Keshavarzi, B., Moore, F., and Lahijanzadeh, A., 2017, Source apportionment and health risk assessment of potentially toxic elements in road dust from urban industrial areas of Ahvaz megacity, Iran: Environmental Geochemistry and Health, p. 1–22, doi: 10.1007/s10653-017-0035-2.

Nassery, H., 1991, Hydrogeological studies of karst springs in the catchment area of Droodzan Dam [MS. thesis]: Shiraz University, (in Farsi).

Pezeshkpour, P., 1991, Hydrogeological and hydrochemical evaluation of Kuh-e Gar-Barm- Firooz springs [MS. thesis]: Shiraz University, (in Farsi).

Plan, L., Decker, K., Faber, R., Wagreich, M., and Grasemann, B., 2009, Karst morphology and groundwater vulnerability of high alpine karst plateaus: Environmental Geology, v. 58, p. 285–297, doi: 10.1007/s00254-008-1605-5.

Raeisi, E., and Kowsar, N., 1997, Development of Shahpour Cave, southern Iran: Cave and Karst Science, v. 24, p. 27–34.

Rahnemaaie, M., 1994, Evaluation of infiltration and runoff in the karstified carbonatic rocks [MS. thesis]: Shiraz, University of Shiraz, (in Farsi).

Rugh, D.F., and Burbey, T.J., 2008, Using saline tracers to evaluate preferential recharge in fractured rocks, Floyd County, Virginia, USA: Hydrogeology Journal, v. 16, p. 251–262, doi: 10.1007/s10040-007-0236-3.

Sepehr, M., and Cosgrove, J.., 2004, Structural framework of the Zagros Fold–Thrust Belt, Iran: Marine and Petroleum Geology, v. 21, p. 829–843, doi: 10.1016/j.marpetgeo.2003.07.006.

Sherkati, S., and Letouzey, J., 2004, Variation of structural style and basin evolution in the central Zagros (Izeh zone and Dezful Embayment), Iran: Marine and Petroleum Geology, v. 21, p. 535–554, doi: 10.1016/j.marpetgeo.2004.01.007.

Sherkati, S., Molinaro, M., Frizon de Lamotte, D., and Letouzey, J., 2005, Detachment folding in the Central and Eastern Zagros fold-belt (Iran): salt mobility, multiple detachments and late basement control: Journal of Structural Geology, v. 27, p. 1680–1696, doi: 10.1016/j.jsg.2005.05.010.

Shipton, Z.K., Evans, J.P., and Thompson, L.B., 2005, The geometry and thickness of deformation-band fault core and its influence on sealing characteristics of deformation-band fault zones: Aapg Memoir, v. 85, p. 181–195, doi: 10.1306/1033723M853135.

Solum, J.G., and Huisman, B.A.H., 2016, Toward the creation of models to predict static and dynamic fault-seal potential in carbonates: Petroleum Geoscience, p. petgeo2016-044, doi: 10.1144/petgeo2016-044.

Stocklin, J., 1968, Structural historiy and tectonics of Iran: A review: The American Association of Petroleum Geologists Bulletin, v. 52, p. 11258–12229.

Surrette, M.J., and Allen, D.M., 2008, Quantifying heterogeneity in variably fractured sedimentary rock using a hydrostructural domain: Geological Society of America Bulletin, v. 120, p. 225–237, doi: 10.1130/B26078.1.

Tesei, T., Collettini, C., Viti, C., and Barchi, M.R., 2013, Fault architecture and deformation mechanisms in exhumed analogues of seismogenic carbonate-bearing thrusts: Journal of Structural Geology, v. 55, p. 167–181, doi: 10.1016/j.jsg.2013.07.007.

Wermund, E., Cepeda, J.C., and Luttrell, P.., 1978, Regional distribution of fractures in the southern Edwards Plateau and their relationship to tectonics and caves: Bureau of Economic Geology, University of Texas at Austin, 14 p.